ADVANCED MATERIALS
www.advmat.de

A Multimodal Sensory Textile Using Programmable Ferroelectric Nanocomposites

Weixiong Li, Xuran Li, Xiao Xiao, Farid Manshaii, Xiaolan Luo, Guorui Chen, Weizhi Li, Guangzhong Xie, Huiling Tai, Yadong Jiang, Yuanjie Su,* and Jun Chen**

With the rapid advancement of artificial intelligence, multimodal sensing is becoming increasingly important. However, conventional approaches relying on multiple integrated sensors face significant challenges due to power consumption and miniaturization requirements. In response, a wearable multimodal sensory textile (MST) for simultaneous mechanical and thermal sensing is developed. The MST demonstrates exceptional capabilities for concurrent mechanical and thermal tactile sensing, with a pressure sensitivity of 0.9 V N^{-1} and temperature sensitivity of 38.7 pA K^{-1}. This outstanding sensing performance is attributed to the mechanical and thermal reinforcement of the programmable ferroelectric nanocomposite enabled by topological engineering. By combining phase-field simulation with experimental characterization, it is revealed that the alignment of ceramic fillers not only promotes spontaneous polarization and out-of-plane domain fraction under external poling but also establishes bimodal pathways for efficient stress and heat transmission. The programmable arrangement and orientation of ferroelectric oxide fillers, achieved by tuning dielectrophoretic voltage, frequency, and temperature, boost piezoelectric and pyroelectric responses by 114% and 131%, respectively, compared to randomly distributed counterparts. This work offers insights into the underlying mechanism of topological modulation in polymer composites and provides new possibilities for designing high-performance functional materials for multimodal sensing, as well as self-powered multimodal sensors for human–machine interfaces and virtual reality.

1. Introduction

Wearable bioelectronics with perception capabilities are increasingly vital for robotics,[1–5] personalized healthcare,[6–11] human–machine interfaces (HMI),[12–14] and virtual reality (VR).[15–18] The growing demand for multimodal sensation—encompassing tactile, thermal, and mechanical stimuli[2]—stems from how biological systems process environmental cues: temperature receptors detect heat flux during object contact, while mechanoreceptors map spatiotemporal pressure distributions. Recent inspiring advances include high-resolution luminescent skin for mechanical imaging,[19] neural arrays for electrophysiological monitoring,[20] and bidirectional HMI with recognition capabilities.[21] However, current systems integrating discrete sensing units[4] face fundamental constraints in miniaturization and power efficiency.[5] To overcome these limitations, we introduce a wearable multimodal sensory textile (MST) that unifies mechanical and thermal perception through programmable ferroelectric nanocomposites.

Wearable electronics typically require electronic films to enable surrounding perception and personalized healthcare monitoring.[7] However, dense functional films suffer from bulkiness, impermeability, and power supply restrictions, necessitating the development of breathable and stretchable electronic devices to ensure comfort and biocompatibility.[8–10] Recent advances in textile-integrated sensing provide promising solutions, with Arief et al. demonstrating how micro/nanostructures in polydimethylsiloxane (PDMS) and fluor-elastomers significantly enhance triboelectric outputs for self-powered sensing.[22] Similarly, Mandal et al. developed self-repairable piezoresistive-triboelectric sensors using natural rubber composites with dynamic networks, addressing durability limitations in harsh environments.[23]

Benefiting from their intrinsic attributes of softness, breathability, mechanical durability, and low cost, integrating sensing and transducing capabilities into wearable textiles could be a powerful and pervasive route to achieve accurate and continuous in situ clinical monitoring and intervention.[12–15] Meena et al. notably achieved exceptional stretchability and high-power density (2.20 mW cm^{-2}) using 3D-printed hybrid piezoelectric-triboelectric nanogenerators with PDMS/BTO layers, enabling real-time tire tread monitoring and highlighting the industrial scalability of polymer–ceramic composites.[24]

W. Li, X. Li, X. Luo, W. Li, G. Xie, H. Tai, Y. Jiang, Y. Su
State Key Laboratory of Electronic Thin Films and Integrated Devices
School of Optoelectronic Science and Engineering
University of Electronic Science and Technology of China
Chengdu 611731, P. R. China
E-mail: leewz@uestc.edu.cn; yjsu@uestc.edu.cn

X. Xiao, F. Manshaii, G. Chen, J. Chen
Department of Bioengineering
University of California, Los Angeles
Los Angeles, CA 90095, USA
E-mail: jun.chen@ucla.edu

The ORCID identification number(s) for the author(s) of this article can be found under https://doi.org/10.1002/adma.202507169

DOI: 10.1002/adma.202507169

Polymers offer flexibility, scalability, and biocompatibility with human skin, but their low energy conversion efficiency significantly restricts their application in wearable electronics. To address this, an efficient and facile approach is the development of ceramic–polymer composites, which combine the energy-harvesting capabilities of ceramics with the flexibility of polymers.[25–30] However, the stiffness mismatch between the two phases hinders load transfer at interfaces, restraining electromechanical coupling efficiency and signal transduction.[31,32] Additionally, the disparity in thermal conductivity between the two phases impedes heat transmission from the polymer matrix to the ceramic fillers, limiting pyroelectric performance in existing composites.[33] Consequently, most existing ceramic–polymer composites lack efficient paths for stress and heat transmission to evoke piezoelectric and pyroelectric responses in ceramic fillers. Ferroelectric nanocomposites are chosen to overcome these limitations and enable self-powered operation due to their inherent energy transduction capabilities[29] and the tunability of their properties through topological engineering.[30]

Here, we report a wearable MST capable of simultaneous and self-powered mechanical and thermal perception. Through topological engineering, we have developed a programmable ferroelectric nanocomposite based on a Sm-PMN-PT/PDMS material system. This composite enables precision tailoring of stress and heat transfer capabilities via electric field manipulation (EFM). By combining phase-field simulations[26] with experimental characterization, we demonstrate that the oriented arrangement of ceramic fillers promotes spontaneous polarization and out-of-plane domain fraction under external poling. This arrangement concurrently improves the piezoelectric response by 114% and the pyroelectric response by 131% compared to the untreated, randomly distributed version at a fixed filler volume fraction. We found that the electric field and frequency of EFM positively affect these performances, while the treating temperature has a negative effect. This work sheds light on the fundamental mechanisms of topological engineering for designing and optimizing ferroelectric nanocomposites. It offers new possibilities for multifunctional self-powered detection, particularly in HMIs and VR applications.

2. Results and Discussion

An ultra-sensitive and highly precise MST based on a programmable ferroelectric nanocomposite is designed to continuously transduce subtle mechanical and thermal stimuli into electrical signals for human–computer interaction, as shown in **Figure 1a**. The proposed MST comprises a typical sandwich structure laminated with polyimide (PI) film, copper (Cu) foils, Sm-PMN-PT ceramic fillers, and a PDMS matrix, as illustrated in Figure 1b. The outermost PI film serves as a protective and electrically insulating layer, while the intermediate Cu foils function as electrodes to collect transferring electrons as output signals. In this work, Sm-PMN-PT ceramic is chosen for sensory fillers due to its ultrahigh piezoelectric coefficient (≈1500 pC N^{-1}) and spontaneous polarization, while PDMS is selected as the polymer matrix for its excellent flexibility and curing traits. The proposed MST uses ferroelectric oxide fillers to simultaneously achieve both mechanical and thermal sensing functionalities in a single device, whereas conventional approaches require separate sensors for force and temperature detection. This integration greatly simplifies the device structure.

The pressure and temperature sensing principles of the MST are illustrated in Figure 1c, where the piezoelectric and pyroelectric effects of ferroelectric ceramic respectively convert mechanical and thermal stimuli into electrical signals. In the absence of pressure and temperature stimuli, the electric dipoles are neutralized by free charges on the electrodes due to electrostatic induction, resulting in no change in spontaneous polarization ($\Delta P = 0$) and no charge transfer in the external circuits. Once force and heat are applied to the Sm-PMN-PT/PDMS composite-based MST, the compression or transverse wobbling of the electric dipoles occurs, and the spontaneous polarization decreases ($\Delta P < 0$), leading to a redistribution of charge between the two electrodes and a forward output current in the external circuit. Conversely, as the force and heat are removed from the MST, the compressed or wobbled dipoles return to their initial state, triggering an enhanced spontaneous polarization ($\Delta P > 0$) and thus a reverse output current.

The spatial distribution and interconnectivity of additive ceramic particles within polymer matrices dominate the electromechanical coupling ability and energy conversion efficiency of composites. Given the superior stiffness and thermal conductivity of ceramic fillers compared to polymer, the arrangement of ceramic fillers plays a crucial role in determining the piezoelectric and pyroelectric activities. Under dielectrophoresis (DEP), the time-varying non-uniform electric field induces dipolar interactions in ferroelectric particles, driving their alignment into chain-like structures parallel to the applied field direction (Figure 1d; Note S1 and Figure S1, Supporting Information). This creates bimodal pathways for efficient stress and heat transmission through the composite. Specifically, unequal positive and negative charges are induced on opposite sides of each ceramic particle. The resulting mutual electrostatic attraction causes adjacent particles to align linearly along the electric field vector (Figures S2 and S3, Supporting Information).[34]

To comprehensively understand the dependence of microstructure evolution on material constants, phase-field simulation was employed to investigate the mechanical and thermal properties of the MST during DEP-induced manipulation of filler dispersion—from initial random distribution, through intermediate assembly, to final alignment. Detailed material constants and Landau coefficients are provided in Tables S1 and S2 (Supporting Information). The DEP-induced microstructural evolution from random to aligned configuration monotonically increases the vertical stiffness (c_{33}) and reduces the horizontal stiffness (c_{11}) (Figure 1e). This directional dependence arises because unidirectional alignment of ceramic fillers along the DEP electric field shortens vertical gaps while widening horizontal distances between particles, compared to random distribution. Given that the ceramic has significantly greater stiffness than the polymer, this alignment enhances the average stiffness (c_{33}) along the vertical direction but reduces it horizontally (c_{11}). As a result, this improved stress transmission capability progressively enhances the piezoelectric charge coefficient (d_{33}) and voltage coefficient (g_{33}) as the microstructure transitions from random to assembled and finally to aligned (Figure 1f and Figure S4, Supporting Information).

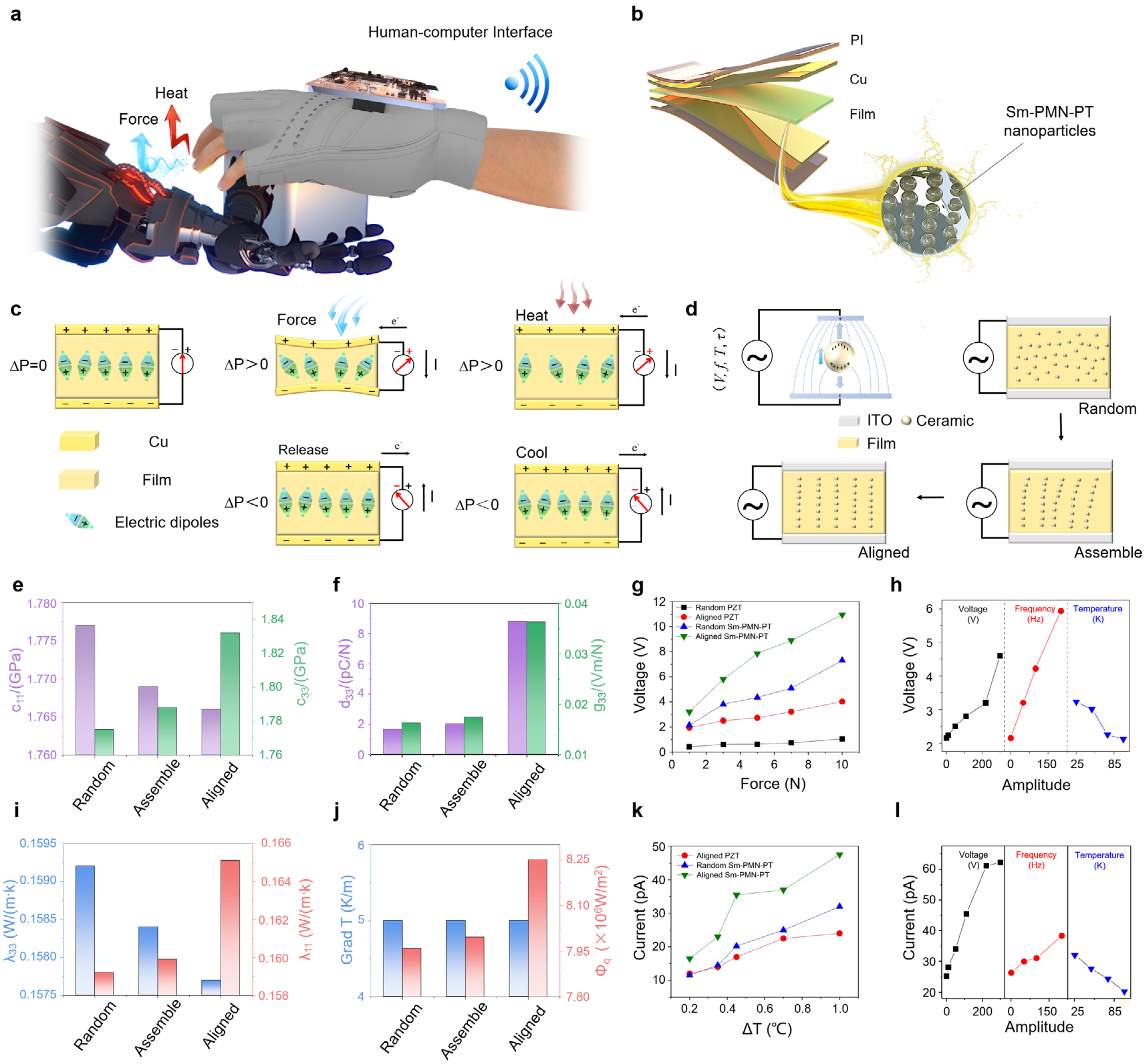

Figure 1. A wearable multimodal sensory system based on the programming ferroelectric nanocomposite. a) Dual-functional programmable ferroelectric nanocomposite-based MST for wearable VR. b) Schematic of the MST comprising a typical sandwich structure. c) Pressure and temperature sensing principles of MST-based electronic skin. d) Alignment of ceramic particles by dielectrophoretic (DEP) effect. e,f) Phase-field simulated stiffness (e) and piezoelectric coefficient (f) of MSTs in response to microstructure evolution from random mode to aligned mode during DEP. g) Dependence of actual measured piezoelectric voltage output of as-prepared MSTs on DEP manipulation and ceramic category. h) Dependence of piezoelectric activity of as-prepared MSTs on the electric field, frequency, and temperature of DEP. i,j) Phase-field simulated thermal conductivity (i) and heat flux density (j) of MSTs in response to the microstructure evolution from random mode to aligned mode during DEP. k) Dependence of actual measured pyroelectric current output of as-prepared MSTs on DEP manipulation and ceramic category. l) Dependence of pyroelectric activity of as-prepared MSTs on the electric field, frequency, and temperature of DEP.

To explore the influence of DEP-induced microstructure evolution on the piezoelectric output performance of as-synthesized MSTs, the output voltages of random and aligned mode ceramic–polymer composite-based MSTs were measured under various stress conditions, as illustrated in Figure 1g. Both Sm-PMN-PT/PDMS and PZT/PDMS composites show significant augmentation in their output performance after DEP alignment compared with their random counterparts. Interestingly, the random mode Sm-PMN-PT/PDMS composite outputs a larger electric signal than the aligned mode PZT/PDMS composite due to its superior piezoelectricity ($d_{33} \approx 1500$ pC N^{-1}) compared to that of ($d_{33} \approx 560$ pC N^{-1}).[35] Since DEP alignment driving force depends on electric field amplitude, frequency, and temperature, we systematically tested the piezoelectric and pyroelectric response of MSTs under these parametric conditions (Note S2, Supporting Information). Output voltage/current scale proportionally with DEP voltage (0–300 V), exhibiting 120% and 150% enhancements at 300 V versus the random comparison (0 V), respectively (Figure 1h; Figure S5a,b, Supporting Information). Performance also rises with DEP frequency (peaking at 200 Hz), where signals exceed the random comparison by 2.7× due to stronger mean aligning fields (Figure 1h; Figure S5c,d, Supporting Information). Conversely, higher curing temperatures reduce output by shortening PDMS solidification time—inhibiting filler alignment and degrading stress transfer (Figure 1h; Figure S5e,f, Supporting Information).

Conversely, in terms of thermal properties, both the calculated heat conductivity coefficient (λ_{33}) and thermal flux density gradually rise as the microstructure evolves from random mode to assembly mode and finally to aligned mode during DEP (Figure 1i,j). The alignment of ceramic fillers boosts the pyroelectric output compared to its random counterpart, regardless of temperature change amplitude (Figure 1k). This is attributed to the chain-like arrangement of ceramic particles, which builds up the thermal conduction pathway. Figure 1l and Figure S6 (Supporting Information) illustrate the dependence of pyroelectric outputs of as-prepared MSTs on the voltage, frequency, and temperature of DEP treatment. With increasing applied voltage, the pyroelectric output of the as-developed MSTs increases, achieving a gain of 146% at 300 V (Figure S6a, Supporting Information). Moreover, the pyroelectric outputs of the MSTs continuously augment with greater frequency (Figure S6b, Supporting Information). Intriguingly, pyroelectricity follows a similar tendency as piezoelectricity in response to DEP voltage and frequency. This confirms that DEP voltage and frequency function as driving forces in the unidirectional arrangement of ceramic particles as the thermal conduction route. However, the amplitude of the output current is inversely proportional to the DEP temperature (Figure 1l and Figure S6c, Supporting Information), which is analogous to the trend of the piezoelectric output, as PDMS tends to solidify at elevated temperatures. Impressively, when the temperature finally rises to 100 °C, the pyroelectric output of the prepared MSTs almost declines to the level of the untreated counterpart. Optimal performance at 25 °C/300 V/200 Hz aligns with governing principles: $F_{\mathrm{DEP}} \propto \nabla \mathrm{E}^2$ (dielectrophoretic force)[36] and $t_{\mathrm{cure}} \propto \mathrm{e}^{\mathrm{Ea}/(\mathrm{RT})}$ (curing kinetics)[37] (Note S2, Supporting Information).

For the sensor with optimized parameters, temperature sensing achieves lower/upper limits of 0.05 K (SNR = 10 dB) and 55 K ($R^2 = 0.995$) (Figures S7 and S8, Supporting Information), while mechanical force sensing ranges from 0.01 N (SNR = 17.5 dB) to 20 N ($R^2 = 0.98$) (Figures S9 and S10, Supporting Information). Dynamic response analysis demonstrates real-time capability with piezoelectric rise/fall times of 0.04/0.13 s and pyroelectric rise/fall times of 0.12/1.54 s (Figure S11, Supporting Information).

To characterize the microstructure evolution during DEP, a scanning electron microscope-backscattered electron (SEM-BSE) was implemented, as displayed in the first column of **Figure** 2a–c. Quantitative orientation analysis (Note S3, Supporting Information) confirms electric-field–driven ordering, with the orientation factor gradually increasing. Clearly, the spatial dispersion of ceramic fillers within the PDMS matrix gradually transforms from random (0 V) to assembly (110 V) and finally alignment (220 V) along the electric field during DEP, establishing chain-like ceramic topology within the polymer for both mechanical and thermal transmission.

In contrast, particle aggregation was observed at a high temperature of 100 °C (Figure S12, Supporting Information). This is because the PDMS solidifies so rapidly at elevated temperatures that ceramic fillers lack sufficient time to arrange in a chain-like manner. The X-ray diffraction (XRD) pattern of as-synthesized MST confirms the polycrystalline perovskite structure of Sm-PMN-PT with high crystallinity (Figure S13, Supporting Information).[38] A typical peak at 536 cm^{-1} in the Fourier transform infrared spectrum suggests the B—O (B = Mg, Nb, Zr, and Ti) stretching normal vibration mode along the spontaneous polarization in the Sm-PMN-PT structure (Figure S14, Supporting Information).[39] High-resolution TEM (HR-TEM) revealed well-defined lattice fringes with 0.284 nm spacing corresponding to the (110) plane (Figure S15, Supporting Information),[34] while XPS analysis confirmed $\mathrm{Sm}^{3+}/\mathrm{Sm}^{2+}$ coexistence and oxygen vacancy formation (Figure S16, Supporting Information).[40]

To quantitatively understand the relationship between ceramic spatial distribution and material properties, a phase-field simulation of effective properties was performed to analyze the impact of dispersion discrepancy on the mechanical and piezoelectric characteristics of the developed MSTs. To mimic the observed DEP-induced microstructural evolution, three types of configurations with random, assembly, and aligned distributions of ceramic fillers were created by computational models at a constant volume fraction of 2.6%, as illustrated in the second column of Figure 2a–c. The material constants of the ceramic filler and polymer matrix are listed in Note S4 (Supporting Information). We visualized 3D mapping of the stress, piezoelectric field, and piezoelectric potential of three types of MSTs under a constant stress of 1 MPa along the z-axis. For the random and assembly configurations (3rd column in Figure 2a,b), the stress mainly concentrates on the interfaces of the ceramic filler and polymer matrix, while most of the external mechanical force dissipates in the polymer matrix and cannot reach the embedded piezoceramic. This results in an inferior potential (fourth column in Figure 2a,b). In contrast, the aligned chains of ceramic particles establish efficient stress transfer pathways to deliver the external load to the appressed ceramic fillers (Figure 2c), compared with their random and assembly counterparts (Figure 2a,b), considerably facilitating the electromechanical coupling efficiency.

The dependence of thermal traits on the microstructure evolution was quantitatively and visually revealed in the fifth and sixth columns of Figure 2a–c. Under a 5K temperature gradient, heat transfer concentrates on the ceramic particle-aligned axon-like channel rather than the polymer matrix, creating a heat conduction pathway. Since the pyroelectric current response of a material ($I = p\frac{\partial T}{\partial t}$) is proportional to the rate of temperature change ($\frac{\partial T}{\partial t}$),[41] the faster temperature-changing rate of pyroelectric material at a constant temperature gradient result in a greater pyroelectric current response. It is worth noting that the pyroelectricity of the as-prepared MSTs comes entirely from the Sm-PMN-PT particles. The enhanced heat transmission through chain-like aligned ceramic particles remarkably promotes the pyroelectric response of the composite films.

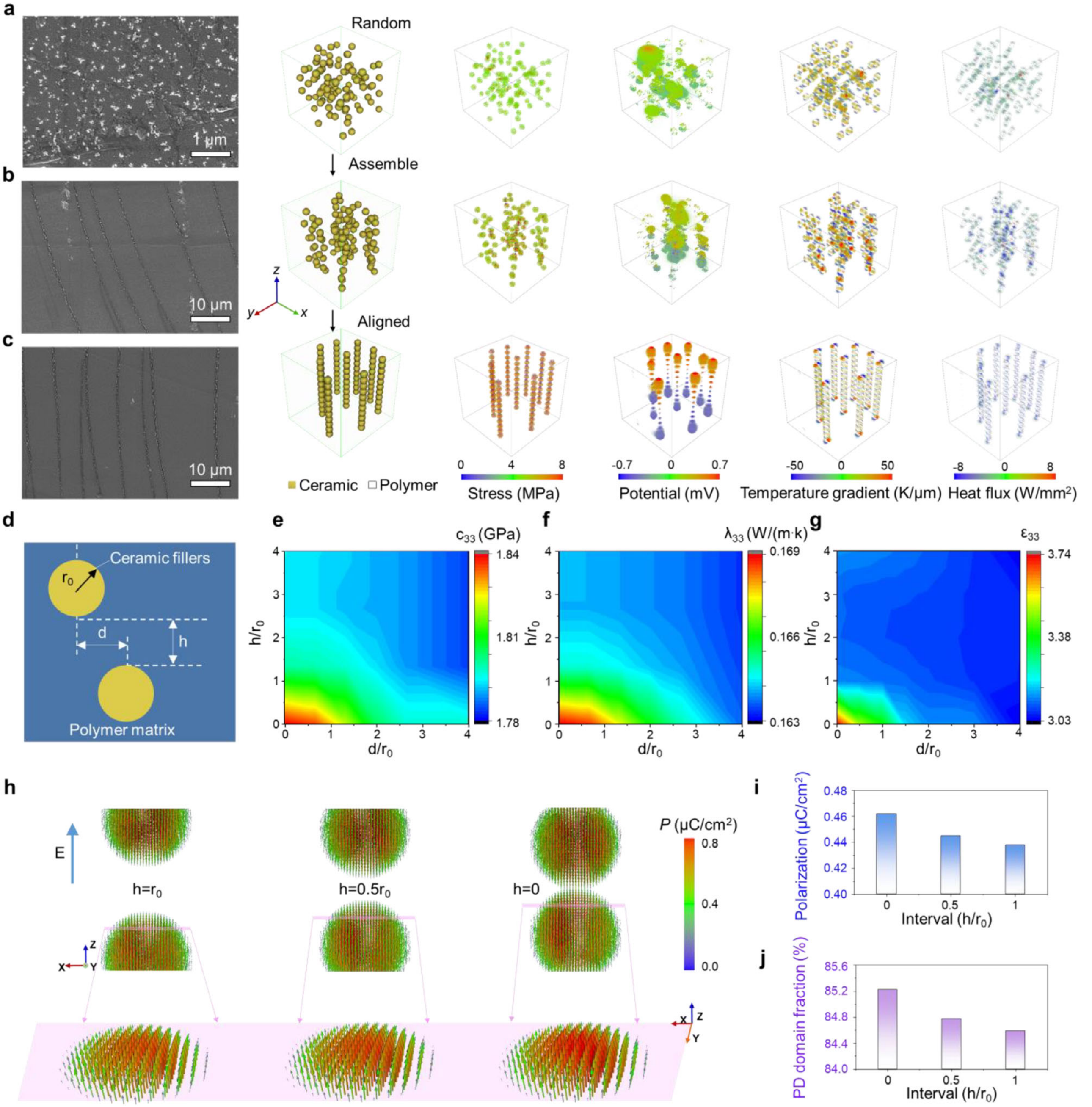

Figure 2. Characterization and understanding of the programming ferroelectric nanocomposite. a–c) SEM-BSE image and phase-field simulation results for MSTs with (a) random, (b) assemble, and (c) alignment dispersion of ceramic nanoparticles. Note: SEM-BSE image (first column), the structural modeling (second column), stress distribution (third column), piezoelectric potential distribution (fourth column), temperature gradient (fifth column), and heat flux (sixth column) of prepared MSTs. d) Dispersing ratios describe the dispersion of ceramic fillers within the polymer matrix. e–g) Simulated e) elastic stiffness (c_{33}), f) thermal conductivity coefficient (λ_{33}), and g) relative permittivity (ε_{33}) as a function of filler dispersion patterns. h) Simulated polarization field within the ceramic particles and (bottom panels) a selected cross section with a fixed distance of 0.375 r_0 from the vertex under different *h* from 0 to r_0. i,j) Simulated spontaneous polarization (i) and poling direction (PD) domain fraction (j) of the selected cross section in (h) as a function of the interval *h*.

The above discussion and comparison cover only three typical topological modes. To achieve universal coverage of possible distribution patterns, a high-throughput computing dataset of various particle dispersion modes was generated by tuning the dispersing ratios of d/r_0 and h/r_0 among ceramic nanoparticles from 0 to 2 (Figure 2d), containing nine typical dispersing patterns to efficiently represent the discrepancy of ceramic filler distribution (Figure S17, Supporting Information). Figure 2e–g illustrates the calculated mechanical, thermal, and dielectric properties of the composites as a function of dispersing ratios. Notably, the effective elastic stiffness (c_{33}), thermal conductivity coefficient (λ_{33}), and dielectric permittivity (ε_{33}) vary continuously with the disparate dispersing ratios (i.e., d/r_0 *and* h/r_0). As the dispersion of these two nanoparticles changes from diagonal distribution (S9) with the largest spacing to vertically seamless alignment (S1), the elastic stiffness (c_{33}), thermal conductivity coefficient (λ_{33}), and dielectric permittivity (ε_r) increase monotonically from 1.790 to 1.844 GPa, from 0.1633 to 0.1684 W $\text{m}^{-1}\text{K}^{-1}$, and from 3.067 to 3.742, respectively. Interestingly, the elastic stiffness follows a trend similar to the thermal conductivity coefficient upon topological evolution, irrespective of additive materials (Figures S18–S25, Supporting Information), implying that modulation of the spatial arrangement of fillers can serve as a universal strategy to tailor the stress and heat conduction of various ceramic–polymer composites. This universal strategy is made possible by our previously developed high-throughput computational platform, which maps tunable stiffness and electromechanical responses to structural evolution,[15] enabling the reverse design of composites for specific applications.

While ideal alignment enhances properties, practical fabrication may introduce localized inhomogeneities. Phase-field simulations quantitatively reveal that defects disrupting filler connectivity (e.g., 10 vol% voids) cause disproportionate degradation: piezoelectric coefficient d_{33} and polarization P_z drop ≈40% due to interrupted charge-transfer pathways, whereas elastic modulus c_{33} and thermal conductivity λ_{33} decrease only ≈10% as these properties remain polymer-dominated (Figure S26, Supporting Information). Visualized potential barriers in defective regions (Figure S27, Supporting Information) confirm microstructural discontinuities critically impede electromechanical coupling.

Poling is a commonly used post-treatment technique to align the domains of ceramic along the direction of the applied electric field. For most ceramic–polymer composites, the large discrepancy in dielectric permittivity between ceramic fillers and the polymer matrix significantly weakens the electric field applied to ferroelectric ceramics during electric poling.[42,43,35] Internal field distribution: $E_{\text{ceramic}}/E_{\text{applied}} = \varepsilon_{\text{polymer}}/\varepsilon_{\text{ceramic}}$, showing high-ε polymers concentrate more field in ceramics (Note S5, Supporting Information).[44,45]

This is unfavorable for consistent domain orientation and polarization enhancement, resulting in poor ferroelectricity.[46] Herein, we performed phase-field simulations of the ferroelectric domain structure to explore whether the domain orientation and switching behaviors during poling can be effectively modulated by the spatial arrangement of ceramic fillers (Figure 2h–j). Under a constant poling electric field of 1 MV m^{-1}, with decreasing intervals between adjacent ceramic particles (Figure 2h), the spontaneous polarization and out-of-plane domain fraction of composites in the poling direction (PD) are gradually enhanced (Figure 2i,j), indicating the possibility of boosting the piezoelectricity ($d_{33} = 2P_s Q_{33}\varepsilon_{33}$)[25] and pyroelectricity ($p = \frac{dP}{dT}$).[16] Moreover, the parallel alignment along the electric field accelerates the domain orientation of the embedded ceramic filler during electric poling, resulting in superior spontaneous polarization compared with the randomly dispersed version (Figure S28, Supporting Information).

With excellent piezoelectric and pyroelectric attributes, MSTs can be utilized for multifunctional sensing applications. The synergistic piezoelectric and pyroelectric responses enable MSTs to operate as self-powered sensors for multifunctional tactile perception. The simultaneous mechanical and thermal signal generation capability provides sufficient output, demonstrating practical self-powered operation. As shown in **Figure 3a**, and Figures S29 and S30 (Supporting Information), under identical conditions, the piezoelectric, pyroelectric, and piezo-pyroelectric coupled outputs of MSTs are all higher than those of thin films with randomly oriented ceramic particles. A piezoelectric output of 0.29 V was obtained for MSTs under impacting-releasing cycles of 0.2 N, while a pyroelectric output of 0.56 V was achieved under heating–cooling cycles with a ΔT of 8 °C. Accordingly, simultaneous mechanical and thermal stimuli generate a combined output voltage of 0.85 V, matching the linear superposition of individual pressure and heating responses. This demonstrates additive superposition of piezoelectric and pyroelectric signals without observable crosstalk. Time-domain residuals (μ ≈0.002 V, σ ≈0.005 V) and frequency-domain coherence ($C_{xy}(f)$ >0.95 across 0.03–10 Hz) quantitatively confirm negligible interference between pressure and thermal signals (Note S6, Supporting Information).

Given that exhalation simultaneously carries mechanical and thermal energies, different breathing patterns—including normal, rapid, and deep breathing—can be effectively identified by attaching MSTs to a conventional mask (Figure 3b). Strikingly, the as-prepared MSTs deliver a larger electric output than those with random ceramic dispersion, regardless of the breathing patterns, indicative of the enhanced piezoelectricity and pyroelectricity. To validate the pristine pyroelectric response in detecting breathing behaviors, the as-received MST was attached to a glass plate instead of a stretchable mask to minimize deformation under respiration. Although the pyroelectric signals are weaker than the pure piezoelectric and hybrid signals, the MST still exhibits a larger output intensity compared to the random mode samples (Figure S31, Supporting Information).

To validate the self-powered sensing capability under real-world stimuli, the MST was attached to the bottom of a cup to transduce the mechanical-thermal energy from pouring hot water into readable signals (Figure 3c). At a constant pouring distance of 12 cm, the outputs of both aligned and random mode devices increased with rising temperatures. Notably, the fabricated MSTs delivered much larger outputs compared to the untreated versions, regardless of the water temperature. To decouple mechanical and thermal contributions, using a stepper-motor-controlled pouring system (fixed height = 12 cm, constant tilt velocity). As shown in Figure S32, Supporting Information, identical rising-edge signals (within blue boxes) confirm piezoelectric dominance during initial impact, while progressively lengthened falling edges (within red boxes) explicitly isolate pyroelectric effects during thermal dissipation at varying water temperatures. This further validates the superior pyroelectric response resulting from microstructure modification.

Furthermore, durability testing confirms the MST's long-term stability. The piezoelectric response exhibits <4% attenuation after 10 000 mechanical cycles (Figure S33a, Supporting Information), while the pyroelectric output maintains <1% degradation (Figure S33b, Supporting Information). 21-day monitoring shows piezoelectric and pyroelectric signals with <1% variation (Figure S34a,b, Supporting Information), collectively verifying

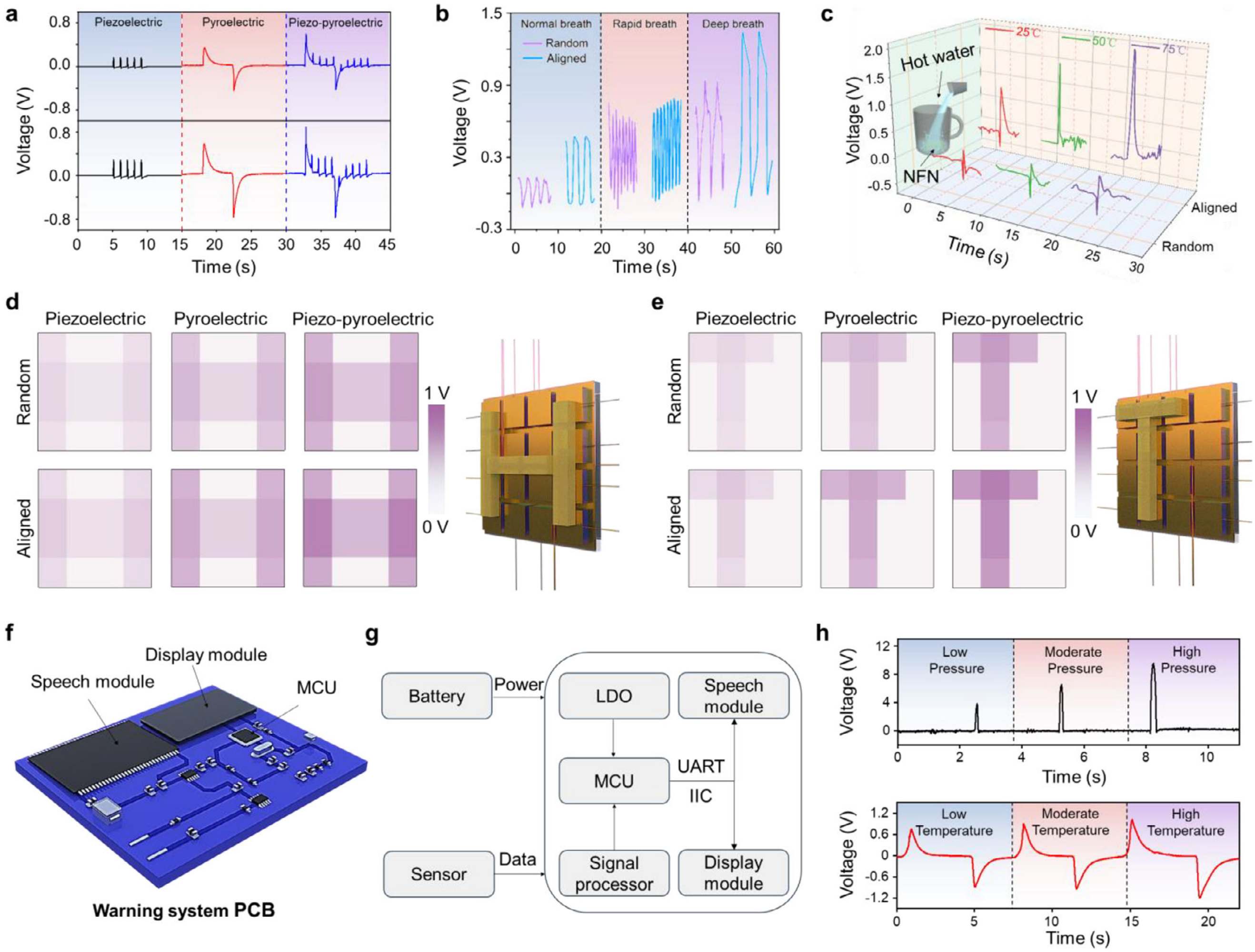

Figure 3. Programming MST for biomechanical to electrical signal conversion. a) The piezoelectric, pyroelectric, and piezo-pyroelectric coupled outputs of as-received MSTs and untreated counterparts. b) Respiratory monitoring is enabled by the prepared MSTs and the untreated random version. c) Simultaneous perception of mechanical force and temperature of poured hot water at different temperatures. d,e) 4 × 4 arrays of MSTs or untreated counterparts recognizing the contacting object with d) "H" shape and e) "T" shape by using various sensing mechanisms. f) Schematic of PCB circuit board and g) circuit diagram of MST-enabled extreme-condition alerting system (MEAS). h) Real-time output waveform of six different conditions distinguished and recognized by MEAS.

robust performance under sustained operational demands. And environmental stability tests confirm the MST's resilience under varying conditions. Under 20–100% RH and 0–80 °C, the output retains >85.3% of baseline performance, demonstrating robustness to environmental variations (Figure S35, Supporting Information).

Benchmarked against state-of-the-art polymer–ceramic composites (Figure S36, Supporting Information), the DEP-aligned MST exhibits superior piezoelectric coefficient (d_{33})[47–57] and pyroelectric coefficient (p),[58–68] achieving simultaneous enhancements unmatched by existing flexible sensors.

To ensure reproducible DEP alignment in scalable fabrication, we implemented two key strategies (Figure S37, Supporting Information): 1) A mosaic array design partitions large-area textiles into smaller independent units (e.g., 2 × 2 cm^2), eliminating PDMS curing gradients and bubble defects that disrupt chain formation in continuous areas; 2) Real-time optical monitoring via transparent ITO electrodes enables rapid laser-scanning detection of alignment inhomogeneities—bubbles increase light transmission while ceramic agglomerations decrease it.

To further demonstrate the potential of MST in HMIs, a 4 × 4 array of MSTs and untreated counterparts were fabricated to identify the shapes of contacting objects. As shown in Figure 3d,e, "H" and "T" shaped wooden blocks were placed on the array. The darker the colors, the higher the peak-to-peak values of the output. It can be observed that the recognition contrast, resolution, and signal-noise-ratio (SNR) of aligned MST devices distinctly surpass those of randomly arranged devices (Figures S38 and S39, Supporting Information). Moreover, the conjugated sensing mode combining pyroelectricity and piezoelectricity enables stronger discerning performance compared to the individual mode due to an additional dimension for shape recognition (Figure S40, Supporting Information).

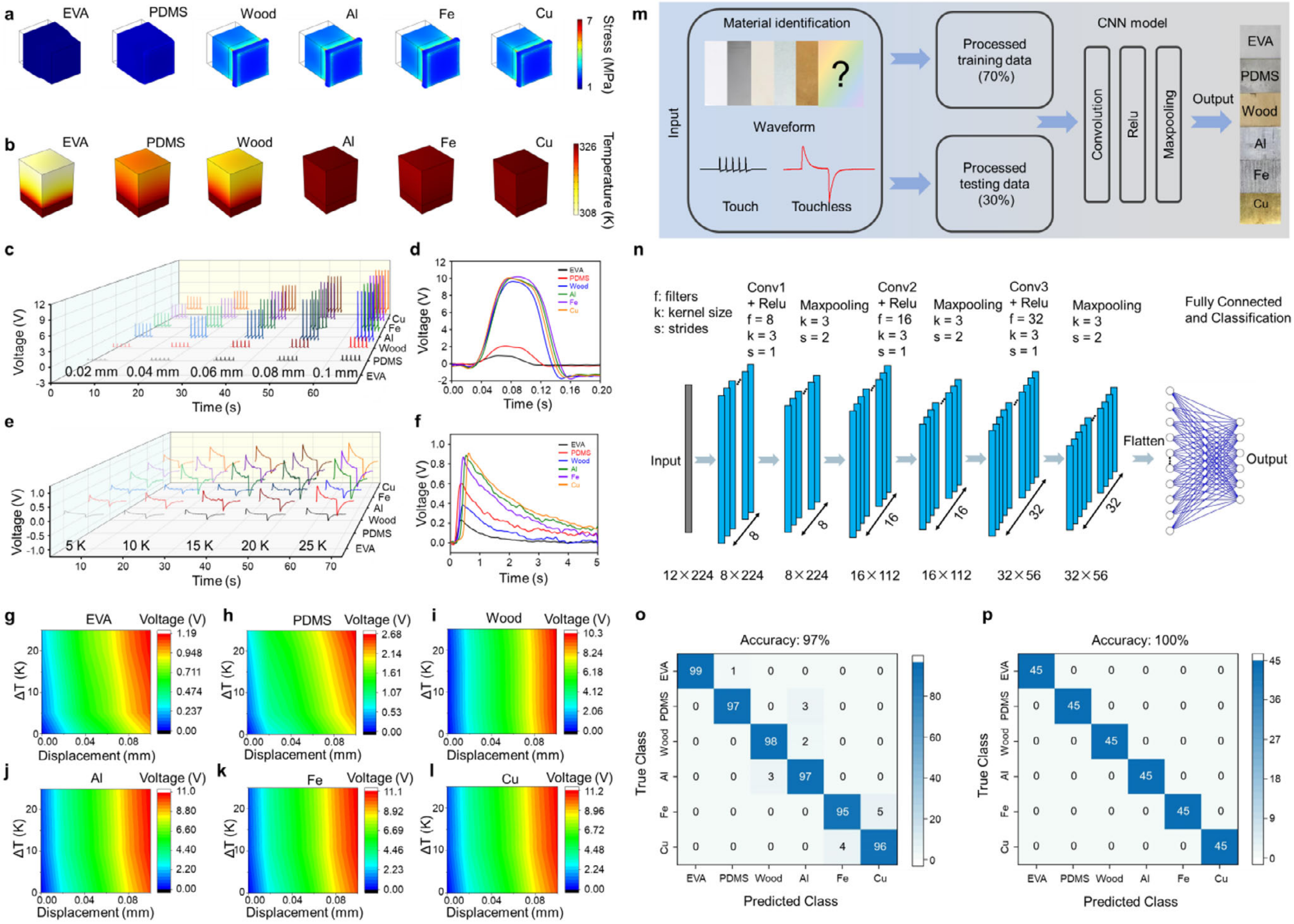

Figure 4. The multimodal sensory textile for self-powered material identification. a,b) Stress (a) and heat (b) transferring traits of different materials simulated by COMSOL. c) Piezoelectric output of MSTs by impacting various materials, and d) a single peak ($\Delta L = 0.1$ mm). e) Pyroelectric output of MSTs in contact with various materials, and f) a single peak ($\Delta T = 25$ K). g–l) Mechanical–thermal dual-modal finger-prints of various materials. m) Flow chart of machine learning for implement differentiation and identification of test materials. n) The algorithmic framework of the CNN. o,p) Classification confusion matrix identified by o) only piezoelectric signals or p) coupled piezoelectric and pyroelectric signals.

Skin perception includes pressure and temperature sensations; however, extreme pressure and temperature stimuli can injure the human body and damage epidermal functions. Figure 3f,g presents the PCB circuit board and electric schematic diagram of the MST-enabled extreme-condition alerting system (MEAS), respectively. Upon receiving electrical signals from the MSTs, the signal processor performs analog-to-digital conversion (ADC) before inputting the data to the microcontroller unit (MCU). The MCU then judges the input force and temperature variables according to predefined thresholds. The as-prepared MEAS can distinguish and identify six different scenarios: low pressure, moderate pressure, high pressure, low temperature, moderate temperature, and high temperature (Figure 3h). Finally, the detected scenario variables can be simultaneously displayed and broadcasted using a display module and a speech module, respectively (Video S1 and S2, Supporting Information). Figure S41 (Supporting Information) shows the design drawings of MEAS. The screen updates every 2 s, displaying "Last moment" (previous measurement) or "At the moment" (real-time value) to avoid ambiguity during loading-free intervals (Figure S42, Supporting Information). Additionally, a LabVIEW-based weighting system integrated with our device enables real-time force value measurement (Note S7 and Video S3, Supporting Information) with an update interval of 0.1 s. Although values are shown to four decimal places, the measurement precision is limited to two decimal places, effectively addressing the limitations of the MEAS.

Skin discerns material categories by coupling temperature and pressure sensations. When in contact with various materials, the pyroelectric output of MSTs is governed by the specific heat capacity and thermal conductivity of the testing materials, while the piezoelectric output of MSTs is dominated by the Young's modulus of the testing materials. These two correlative mechanisms were explicitly unraveled by finite element analysis based on COMSOL simulations (**Figure** 4a,b). In Figure 4a, the material cube's bottom surface is fixed along the y-axis and compressed vertically at a constant deformation by the MSTs (Table S3 and Figure S43a, Supporting Information). It is evident that materials with a higher Young's modulus (like Cu, Fe, Al) render greater stress, while soft materials, such as EVA and PDMS, experience lower stress. Figure 4c displays the piezoelectric output of the as-received MSTs when contacting various materials as a function of deformation. High modulus materials (Cu, Fe, and Al) deliver larger piezoelectric output voltages than low modulus materials (EVA, PDMS) irrespective of applied strains (ΔL = 0.02, 0.04, 0.08, and 0.1 mm) (Figure 4c). This is because the diverse modulus (E) of various materials will differentiate the piezoelectric polarization ($P = d_{33}\sigma = d_{33}E\varepsilon$) at a constant deformation (ε); thus, the piezoelectric output is proportional to the material's modulus in this case. Interestingly, no reverse peaks below 0 V were observed for the low modulus materials of EVA and PDMS (Figure 4d), indicating no film rebound occurs because of their softness. Accordingly, the intensity and waveform of prepared MSTs can be used to distinguish the softness and hardness of materials.

In terms of heat transfer ability, the material cubes were heated at the bottom surface by a heat source along the z-axis, as shown in Figure 4b and Figure S43b (Supporting Information). At thermal equilibrium, metals (Al, Fe, and Cu) exhibit a uniform temperature distribution due to their high thermal conductivity, whereas organic materials like EVA and PDMS exhibit a temperature gradient due to low thermal conductivity. The lower the thermal conductivity, the greater the temperature gradient (Table S4, Supporting Information). When MSTs approach and depart from the heated material cubes without contact, assisted by a linear motor, pyroelectric signals are generated as a result of the time-varying temperature difference ($\partial T/\partial t$) arising from repeated sliding between the heating table and the atmosphere. The high thermal conductivity materials (Cu, Fe, and Al) yield larger pyroelectric output voltages than the low thermal conductivity materials (EVA and PDMS), regardless of temperature variation (ΔT = 5, 10, 15, 20, and 25 K) (Figure 4e,f). Since material cubes with higher thermal conductivity allow the MSTs to absorb more thermal energy, this leads to larger output peaks. Consequently, the thermal conductivity of testing materials can be identified by as-fabricated MSTs according to the pyroelectric output.

By synergizing piezoelectric and pyroelectric output signals, the mechanical-thermal dual-modal fingerprints of different materials among EVA, PDMS, wood, Al, Fe, and Cu were acquired, as depicted in Figure 4g–l and Figure S44 (Supporting Information). Significantly, under various mechanical displacement (X-axis) and temperature variation (Y-axis) conditions, the piezoelectric–pyroelectric bimodal fingerprints vary with varying materials. To this end, we can employ the detected output patterns to differentiate and identify the testing materials via a convolutional neural network (CNN) algorithm (Figure 4m). Figure 4n displays the algorithmic framework of the CNN, composed of an input layer, three convolutional layers, a flattening layer, and a fully connected layer. Each CNN layer consists of a convolutional layer, a ReLU layer, and a max-pooling layer. The input layer normalizes and transitions the preprocessed data into the network. Subsequently, input data is extracted and filtered by the CNN convolution layer and ReLU layer, followed by reduction and merging through the max-pooling layer. The flattening layer receives data from the CNN layer and adjusts its size for the fully connected layer, which integrates features, classifies data, and outputs results. Each layer's convolution kernel is 3×3, with the number of kernels increasing gradually (f = 8, 16, 32). The detailed training and testing processes are discussed in the Experimental Section. This method compresses the data and extracts more features by reducing the matrix resolution and increasing the number of feature layers. Noteworthy, CNN feature maps explicitly isolate piezoelectric (force impact) and pyroelectric (thermal impact) responses, confirming CNN's ability to separate signals (Note S8, Supporting Information).

It is worth noting that the classification confusion matrices achieve an accuracy of 97% for individual piezoelectric signal recognition (Figure 4o and Figure S45, Supporting Information), whereas an overall accuracy of 100% was achieved by coupling piezoelectric and pyroelectric signals in the process of tactile recognition (Figure 4p and Figure S46, Supporting Information). This result indicates that the addition of an extra sense dimension improves the accuracy of material identification. Generalizability tests under real-world noise (Note S9, Supporting Information) confirm robust 92.6% recognition accuracy after physics-guided data augmentation and dropout regularization, overcoming white noise, baseline wander or unstable impacts that degraded lab-only models to 78.9%.

Leveraging the capability of concurrently recognizing mechanical and thermal stimuli, a wearable VR interface was developed to project the texture and temperature information of goods in a virtual shop. As shown in **Figure 5a**, this MST-enabled VR interface consists of a signal generation module, signal processing module, CNN classification module, and VR interface conversion module. The complete workflow of the wearable VR system is illustrated in Figure 5a. Signals captured by MSTs worn on the fingertip are processed—filtered, amplified, and read—by the circuit mounted on the back of the hand, and subsequently transmitted to the computer via Bluetooth. Then, the CNN deep learning algorithm discriminates the category and temperature of the grasped objects by analyzing the piezoelectric and pyroelectric signal characteristics, culminating in VR interaction with the objects in the physical world. Figure 5b displays the real-time piezoelectric waveforms for grasping three different beverages: a coffee plastic cup, a milk paper cup, and a cola can cup at room temperature. Notably, the coffee plastic cup has the largest softness and thus produces the smallest output, while the cola can cup has the largest stiffness and thereby triggers the greatest output. Figure 5c illustrates the pyroelectric output when approaching hot beverages of coffee, milk, and cola at 40 °C. The highest thermal conductivity of the can (cola) triggers the greatest pyroelectric output, followed by plastic (coffee) and paper (milk).

Figure 5d depicts the block diagram of the processing circuit on the back of the hand, with the detailed logic diagram presented in Figure 5e and Figure S47 (Supporting Information). The signals from the fingertip-worn sensor are pre-processed by a filter (FIL) and an amplifier (AMP) via a row of pin lines (HDR), and then transmitted to a microprocessor (MCU) for ADC. The processed data is transmitted to the server (SERVER) through the Bluetooth module (BLE) based on the universal asynchronous receiver/transmitter. An external crystal circuit (XTAL) supplies the clock signal (OSC) to the MCU. The low dropout linear regulator (LDO) stabilizes the operating voltage at 3.3 V to power the MCU.

Signals acquired by this wearable MST were subsequently processed by the CNN deep learning algorithm, achieving an overall classification accuracy of 100% for the recognition of coffee, milk, cola, hot coffee, hot milk, and hot cola, as evidenced by the

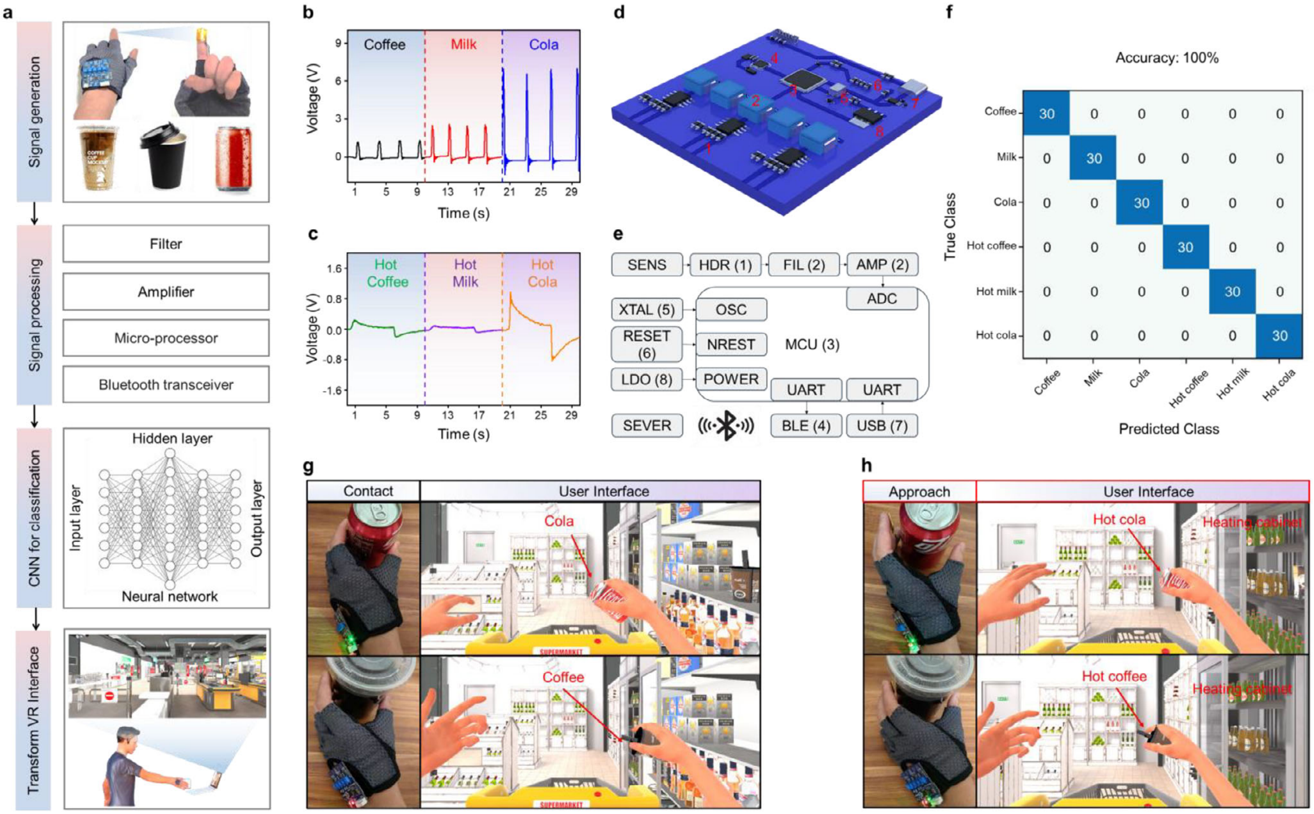

Figure 5. The multimodal sensory textile for wearable virtual reality. a) Workflow of the wearable virtual reality (VR) system. b) Real-time piezoelectric waveforms for grasping three different beverages at room temperature. c) Pyroelectric waveform by approaching various hot beverage. d,e) The block diagram (d) and detailed logic diagram (e) of the processing circuit on the back of the hand. f) Confusion matrix demonstrating the recognition of six drinks. g,h) Wearable VR interface for visually selecting goods by grasping cold drinks (g) and touching hot drinks (h) in physical world.

confusion matrix in Figure 5f and Figure S48 (Supporting Information). The practical application of wearable VR is demonstrated in Figure 5g,h, where the visualized contents were chosen by the Unity3D engine. When physically grasping different kinds of beverages (Figure 5g) including coffee, milk, and cola, the virtual counterpart selects the corresponding items from the shelf in the VR shop (Video S4, Supporting Information). Furthermore, the collection of pyroelectric signals allows the MST to recognize the temperature traits of beverages and virtually select the corresponding hot drinks (coffee, milk, and cola) from the beverage heating cabinet (Figure 5g; Figure S49 and Video S5, Supporting Information). Conversely, it is convenient for shop staff wearing our MST gloves to synchronize the goods shelves of the VR shop when placing goods in real supermarkets.

Notably, all the pressure and temperature detection were conducted in a self-powered manner via the piezoelectric and pyroelectric effects of ferroelectric ceramic fillers, ensuring both low-energy consumption and high integration levels for constructing on-demand e-skin. Most importantly, the piezoelectric tensor (touch sense), pyroelectric coefficient (heat sense), stiffness tensor (conformality), and even domain switching behaviors (excitation conduction) of ceramic-polymer composites-based e-skin can be precisely programmed through DEP, permitting a promising strategy for designing high-performance e-skin and multifunctional wearable sensors.

3. Conclusions

In this work, a programmable ferroelectric nanocomposite-enabled MST was developed via electric field alignment to enhance piezoelectricity and pyroelectricity for pressure and thermal sensing, respectively, as well as domain switching behaviors (excitation conduction). By combining phase-field simulation with experimental characterization, we demonstrated that the alignment of ceramic fillers not only improves spontaneous polarization and out-of-plane domain fraction under external poling but also establishes bimodal pathways for efficient stress and heat transmission. The piezoelectric and pyroelectric responses were enhanced by 114% and 131%, respectively, compared to the untreated randomly distributed version. It was found that the electric field and frequency of DEP have a positive effect, whereas the DEP temperature hurts piezoelectric and pyroelectric performance.

Assisted by CNN for dual signal processing, accurate and rapid object shape and character identification were achieved. Sensory systems with outstanding dual-modal perceptual abilities and cognitive intelligence demonstrate promising applications in the HMI and wearable VR, like in unmanned stores and next-generation online shopping.

This work not only offers insights into the underlying mechanisms of topological modulation/optimization in polymer composite-based e-skin but also provides new possibilities for designing and developing high-performance multifunctional wearable sensory systems.

4. Experimental Section

Dielectrophoresis-Enabled Alignment: The researchers weighed and mixed 25.92 g of Sm-PMN-PT, 10 g of PDMS solution, and 1 g of PDMS coagulant. The mixture was stirred with a glass rod for 15 min to obtain a white slurry. This white slurry was then placed in a vacuum environment and vacuumed until no bubbles remained in the beaker. The white paste was poured into a homemade container sandwiched between two ITO glasses. An alternating current stabilizing power supply was connected to the ITO glasses. The DEP was implemented with tunable voltage, frequency, and temperature to obtain the composite film with a chain-like arrangement of Sm-PMN-PT ceramic particles (Figure S20, Supporting Information).

Preparation of the MSTs: The composite film was cut to a size of 2 × 2 cm^2, and double-sided conductive copper tape was attached to both sides of the composite film as electrodes. The composite film was then placed into an oil bath and polarized under a voltage bias of 1,500 V at 100 °C. The flexible MSTs were connected with lead wires to the copper electrodes and packaged with medical GU film.

Characterization and Measurement: The morphologies of the samples were characterized by an SEM-BSE operated at 20 kV (FEI QuANTA 200, Netherlands). An X-ray diffractometer (XRD: D8 Advance, Bruker-AXS, Germany) equipped with Cu Kα radiation (λ = 1.5418 Å and 2θ = 20–80°) was used to analyze the crystal structure of the samples at room temperature. The FT-IR (Fourier-transform infrared) spectra of the samples were measured by a Fourier infrared spectrometer (IRAffinity-1S, SHIMADZU, Japan). Elemental composition and chemical valence states were characterized using an X-ray photoelectron spectrometer (XPS: K-Alpha+, Thermo Fisher Scientific, USA) equipped with a monochromatic Al Kα X-ray source ($h\nu$ = 1486.6 eV), charge compensation system, and hemispherical energy analyzer. Atomic-scale morphology and crystallographic structure were investigated using a field-emission transmission electron microscope (TEM: Talos F200X, Thermo Fisher Scientific, USA) operated at 200 kV acceleration voltage, achieving a point resolution of 0.25 nm (TEM mode).

A linear motor with tunable frequencies, velocities, and amplitudes was employed to trigger repeated, periodic impacts on the surface of the device to generate a piezoelectric signal. The measurement method for pyroelectric performance involved attaching the sensor to a thermoelectric cooler (TEC) to sense temperature changes. The frequency and amplitude of the changes were achieved by connecting the TEC to a waveform generator and power amplifier. The output voltage and current across the testing sensor were measured by the Keithley 6514 electrometer system, and the data were recorded in real-time by a personal computer with LabVIEW software.

Phase-Field Simulation of the Ferroelectric Domain Structures: In the phase-field simulation, the time-dependent Ginzburg–Landau equation was employed to describe the evolution of the polarization,[69] as follows

$$\frac{\partial P_i(r,t)}{\partial t} = -L\frac{\delta F}{\delta P_i(r,t)},\ (i = 1, 2, 3) \tag{1}$$

where L is the kinetic coefficient, t is the time, F is the total free energy of the system, $\mathbf{r} = (x, y, z)$ is the spatial position vector, and $P_\mathrm{i}(\mathbf{r}, t)$ is the polarization field. Additionally, $\delta F/\delta P_\mathrm{i}(\mathbf{r}, t)$ is the thermodynamic driving force for the spatial and temporal evolution of polarization.

The total free energy of the system includes contributions from the bulk free energy f_bulk, the elastic energy f_elastic, the electrostatic energy f_electric, and the gradient energy f_grad

$$F = \int_V \left[f_\mathrm{bulk} + f_\mathrm{elastic} + f_\mathrm{electric} + f_\mathrm{grad}\right] \mathrm{d}V \tag{2}$$

In particular, the bulk free energy density f_bulk is expressed following the Landau theory. The bulk free energy density of Sm-PMN-PT is written as a sixth-order polynomial[70]

$$\begin{aligned} f_\mathrm{bulk} &= \alpha_1\left(P_x^2+P_y^2+P_z^2\right)+\alpha_{11}\left(P_x^4+P_y^4+P_z^4\right)\\ &+\alpha_{12}\left(P_x^2P_y^2+P_x^2P_z^2+P_y^2P_z^2\right)+\alpha_{111}\left(P_x^6+P_y^6+P_z^6\right)\\ &+\alpha_{112}\left(P_x^2\left(P_y^4+P_z^4\right)+P_y^2\left(P_z^4+P_x^4\right)+P_z^2\left(P_x^4+P_y^4\right)\right)+\alpha_{123}P_x^2P_y^2P_z^2 \end{aligned} \tag{3}$$

where α_i, α_ij, α_ijk are the Landau coefficients. The bulk free energy density of PVDF is expressed as

$$f_\mathrm{bulk} = \alpha_1P_x^2+\alpha_2P_y^2+\alpha_3P_z^2+\alpha_{33}P_z^4+\alpha_{333}P_z^6 \tag{4}$$

This expression is established following a uniaxial anisotropy with spontaneous polarization along the z-axis (the poling direction during electrospinning), described by a sixth-order expansion of P_z, while polarization components along the x and y axes assume paraelectric properties with only second-order terms considered.

The evolution of the domain structure was simulated for a single electrospun fiber under an applied electric field of 1.2 kV cm^{-1}, following the in situ poling field of electrospinning. The simulations were performed in a 3D system with a total size of 512 nm × 512 nm × 512 nm containing two Sm-PMN-PT particles (diameter = 100 nm) in a PDMS matrix, which was discretized into a 3D array of 128 × 128 × 128 grids with a grid size of $\Delta x = \Delta y = \Delta z$ = 4 nm. Periodic boundary conditions were employed for the polarization field, electric field, and mechanical displacement field. The material constants of Sm-PMN-PT and PDMS are listed in Tables S1 and S2 (Supporting Information), respectively. All phase-field simulations in the present work were performed using the Mu-PRO ferroelectric module for Linux cluster software released by Mu-PRO LLC.

Calculation of Effective Properties Regarding Piezoelectric Composites: These simulations were performed using the Mu-PRO Effective Properties module for the Linux cluster released by Mu-PRO LLC to systematically study and compare the stress and heat transfer capabilities, as well as the electromechanical coupling effect, of the as-received MSTs with diverse microstructures. The composite system consisted of randomly oriented Sm-PMN-PT nanoparticles with a diameter of d = 100 nm and a total content of 2.6 vol% in a PDMS matrix. The total system size was 12.8 µm × 12.8 µm × 12.8 µm, which was discretized into a 3D array of 128 × 128 × 128 grids. A 3D periodic boundary condition was employed.

The effective dielectric constant $\varepsilon_r^\mathrm{eff}$ and piezoelectric coefficient d_r^eff of the composite system were calculated by modeling the response of the electric displacement field $D(\mathrm{r})$ and the piezostrain $\varepsilon(\mathbf{r})$ of the composites to a small testing electric field $\boldsymbol{E}_\mathrm{app}$ under a stress-free condition. The material response was simulated by solving the electrostatic and elastic equilibrium equations coupled with linear constitutive relations[71]

$$\nabla\cdot D = \nabla\cdot\left(\varepsilon_0\varepsilon_r E + d\sigma\right) = 0 \tag{5}$$

$$\nabla\cdot\sigma = \nabla\cdot\left(c\varepsilon - cd^T E\right) = 0 \tag{6}$$

where ε_0 is the vacuum permittivity, $\boldsymbol{\varepsilon}_\mathrm{r}(\mathbf{r})$ is the relative dielectric constant of the local phase, $\mathbf{c}(\mathbf{r})$ is the elastic stiffness, and $\mathbf{d}(\mathbf{r})$ is the piezoelectric coefficient. A Fourier-spectral iterative-perturbation method[41,71] was employed to obtain the numeric solution. The effective material properties of the composites were then calculated following $\varepsilon_0\varepsilon_r^\mathrm{eff}E_\mathrm{app} = \langle\Delta D\rangle$ and $\mathbf{d}^{\mathrm{eff}T}E_\mathrm{app} = \langle\Delta\varepsilon\rangle$, where $\langle\Delta\mathbf{D}\rangle$ and $\langle\Delta\varepsilon\rangle$ are the spatial averages of the displacement response and the strain response within the whole system, respectively. The material constants of the Sm-PMN-PT fillers and the PDMS matrix are listed in Note S2 (Supporting Information).

Training and Testing for Machine Learning: The film was pressed by each material cube 100 times, yielding piezoelectric voltage dynamic waveforms. Pyroelectric voltage dynamic waveforms were obtained by approaching the heated material cubes 45 times. For beverage identification, this process was repeated 30 times. Data was captured using a Keithley 6514 electrostatic meter at a sampling frequency of 1000 Hz. The acquired data formed lengthy 1D arrays, with voltage values at 0.001-s intervals and about 300 000 points per cycle, making waveform characteristics challenging to visualize as 2D images. Consequently, the data was converted into waveform images (voltage–time) of ≈810 × 650 pixels using Origin software. An initial database was established with N datasets for piezoelectric, pyroelectric, and beverage recognition (N equaled 100, 45, and 30, respectively). Machine learning was applied to the concept of image recognition. 70% of the datasets were randomly chosen as training samples, with the remaining 30% serving as test samples. A CNN model, based on the PyTorch framework, was developed. The final model converted all data into 1D vectors for waveform classification.

Creation of Wearable Virtual Reality Applications: The sensory system identified the grasped objects, which were then manipulated in a VR environment. 3D modeling software (such as 3ds Max and Blender) was utilized to design and create props and environments, followed by importing the constructed models and animations into the Unity3D engine. A high-resolution display with 1080 × 1200 pixels was used to showcase the entire virtual store. This study does not require ethics committee approval. All human body-related experiments of wearable devices on a volunteer were performed in compliance with the relevant laws. All participants were given written and informed consent before participating in the study.

Supporting Information

Supporting Information is available from the Wiley Online Library or from the author.

Acknowledgements

W.L., X.L., and X.X. contributed equally to the work. Y.S. acknowledges the National Natural Science Foundation of China (Grant No. 62 074 027), the Sichuan Province Hong Kong, Macao and Taiwan Science and Technology Innovation Cooperation Project (Grant No. 2024YFHZ0367), and the Center for HPC, University of Electronic Science and Technology of China. W.L. acknowledges the Natural Science Foundation of Sichuan (Grant No. 2024NSFSC0462). J.C. acknowledges the Henry Samueli School of Engineering and Applied Science and the Department of Bioengineering at the University of California, Los Angeles for the startup support.

Conflict of Interest

The authors declare no conflict of interest.

Data Availability Statement

The data that support the findings of this study are available from the corresponding author upon reasonable request.

Keywords

multimodal sensing, nanocomposites, phase-field simulation, smart textiles, wearable bioelectronics

Received: April 15, 2025
Revised: July 30, 2025
Published online: August 16, 2025

---

[1] Z. Che, X. Wan, J. Xu, C. Duan, T. Zheng, J. Chen, *Nat. Commun.* **2024**, *15*, 1873.
[2] G. Chen, X. Xiao, X. Zhao, T. Tat, M. Bick, J. Chen, *Chem. Rev.* **2022**, *122*, 3259.
[3] X. Zhao, Y. Zhou, Y. Song, J. Xu, J. Li, T. Tat, G. Chen, S. Li, J. Chen, *Nat. Mater.* **2024**, *23*, 703.
[4] J. Yin, S. Wang, T. Tat, J. Chen, *Nat. Rev. Bioeng.* **2024**, *2*, 541.
[5] Y. Zhou, X. Zhao, J. Xu, G. Chen, T. Tat, J. Li, J. Chen, *Sci. Adv.* **2024**, *10*, adj8567.
[6] Y. Su, G. Chen, C. Chen, Q. Gong, G. Xie, M. Yao, H. Tai, Y. Jiang, J. Chen, *Adv. Mater.* **2021**, *33*, 2101262.
[7] Y. Zhou, X. Zhao, J. Xu, Y. Fang, G. Chen, Y. Song, S. Li, J. Chen, *Nat. Mater.* **2021**, *20*, 1670.
[8] Y. Su, C. Chen, H. Pan, Y. Yang, G. Chen, X. Zhao, W. Li, Q. Gong, G. Xie, Y. Zhou, S. Zhang, H. Tai, Y. Jiang, J. Chen, *Adv. Funct. Mater.* **2021**, *31*, 2010962.
[9] T. Zhang, H. Liang, Z. Wang, C. Qiu, Y. B. Peng, X. Zhu, J. Li, X. Ge, J. Xu, X. Huang, J. Tong, J. Ou-Yang, X. Yang, F. Li, B. Zhu, *Sci. Adv.* **2022**, *8*, abk0159.
[10] X. Zhao, Y. Zhou, J. Xu, G. Chen, Y. Fang, T. Tat, X. Xiao, Y. Song, S. Li, J. Chen, *Nat. Commun.* **2021**, *12*, 6755.
[11] Y. Su, W. Li, X. Cheng, Y. Zhou, S. Yang, X. Zhang, C. Chen, T. Yang, H. Pan, G. Xie, G. Chen, X. Zhao, X. Xiao, B. Li, H. Tai, Y. Jiang, L.-Q. Chen, F. Li, J. Chen, *Nat. Commun.* **2022**, *13*, 4867.
[12] Z. Zhou, K. Chen, X. Li, S. Zhang, Y. Wu, Y. Zhou, K. Meng, C. Sun, Q. He, W. Fan, E. Fan, Z. Lin, X. Tan, W. Deng, J. Yang, J. Chen, *Nat. Electron.* **2020**, *3*, 571.
[13] Y. Su, W. Li, L. Yuan, C. Chen, H. Pan, G. Xie, G. Conta, S. Ferrier, X. Zhao, G. Chen, H. Tai, Y. Jiang, J. Chen, *Nano Energy* **2021**, *89*, 106321.
[14] G. Chen, T. Tat, Y. Zhou, Z. Duan, J. Zhang, K. Scott, X. Zhao, Z. Liu, W. Wang, S. Li, K. Cross, J. Chen, *Nat. Chem. Eng* **2025**, *2*, 358.
[15] G. Chen, Y. Fang, X. Zhao, T. Tat, J. Chen, *Nat. Electron.* **2021**, *4*, 175.
[16] X. Zhao, J. Li, Y. Zhou, J. Chen, *Matter* **2022**, *5*, 2590.
[17] Y. Zhou, X. Xiao, G. Chen, X. Zhao, J. Chen, *Joule* **2022**, *6*, 1381.
[18] S. Xiang, G. Chen, Q. Wen, H. Li, X. Luo, J. Zhong, S. Shen, A. Di Carlo, X. Fan, J. Chen, *Matter* **2024**, *7*, 82.
[19] C. Jia, Y. Xia, Y. Zhu, M. Wu, S. Zhu, X. Wang, *Adv. Funct. Mater.* **2022**, *32*, 2201292.
[20] K. J. Seo, M. Hill, J. Ryu, C.-H. Chiang, I. Rachinskiy, Y. Qiang, D. Jang, M. Trumpis, C. Wang, J. Viventi, H. Fang, *npj Flex. Electron.* **2023**, *7*, 40.
[21] P. Fang, M. Zhu, Z. Zeng, W. Lu, F. Wang, L. Zhang, T. Chen, L. Sun, *Adv. Funct. Mater.* **2024**, *34*, 2310254.
[22] I. Arief, P. Zimmermann, S. Hait, H. Park, A. K. Ghosh, A. Janke, S. Chattopadhyay, J. Nagel, G. Heinrich, S. Wießner, A. Das, *Mater. Horiz.* **2022**, *9*, 1468.
[23] S. Mandal, I. Arief, S. Chae, M. Tahir, T. X. Hoang, G. Heinrich, S. Wießner, A. Das, *Adv. Sensor Res.* **2024**, *3*, 2400036.
[24] K. K. Meena, I. Arief, A. K. Ghosh, H. Liebscher, S. Hait, J. Nagel, G. Heinrich, A. Fery, A. Das, *Nano Energy* **2023**, *115*, 108707.
[25] F. Li, S. Zhang, T. Yang, Z. Xu, N. Zhang, G. Liu, J. Wang, J. Wang, Z. Cheng, Z.-G. Ye, J. Luo, T. R. Shrout, L.-Q. Chen, *Nat. Commun.* **2016**, *7*, 13807.
[26] Z.-H. Shen, J.-J. Wang, J.-Y. Jiang, S. X. Huang, Y.-H. Lin, C.-W. Nan, L.-Q. Chen, Y. Shen, *Nat. Commun.* **2019**, *10*, 1843.
[27] Z. Shen, J. Wang, Y. Lin, C. Nan, L. Chen, Y. Shen, *Adv. Mater.* **2018**, *30*, 1704380.
[28] Z.-H. Shen, Z.-W. Bao, X.-X. Cheng, B.-W. Li, H.-X. Liu, Y. Shen, L.-Q. Chen, X.-G. Li, C.-W. Nan, *npj Comput. Mater.* **2021**, *7*, 110.
[29] S. Peng, X. Yang, Y. Yang, S. Wang, Y. Zhou, J. Hu, Q. Li, J. He, *Adv. Mater.* **2019**, *31*, 1807722.
[30] G. Belijar, S. Diaham, Z. Valdez-Nava, T. Lebey, *J. Phys. D: Appl. Phys.* **2015**, *49*, 045501.
[31] J. Burger, S. C. Meepagala, E. L. Wolf, *Rev. Sci. Instrum.* **1989**, *60*, 735.
[32] V. Morales-Flórez, A. Domínguez-Rodríguez, *Prog. Mater. Sci.* **2022**, *128*, 100966.

[33] R. Ram, V. Soni, D. Khastgir, *Composites, Part B* **2020**, *185*, 107748.
[34] L. Gu, J. Liu, N. Cui, Q. Xu, T. Du, L. Zhang, Z. Wang, C. Long, Y. Qin, *Nat. Commun.* **2020**, *11*, 1030.
[35] C. J. Dias, D. K. Das-Gupta, *IEEE Trans. Dielect. Electr. Insul.* **1996**, *3*, 706.
[36] Y. Yang, S. Biswas, R. Xu, X. Xiao, X. Xu, P. Zhang, H. Gong, X. Zheng, Y. Peng, J. Li, H. Ai, Y. Wu, Y. Ye, X. Gao, C. Serrao, W. Zhang, P. Sayavong, Z. Huang, Z. Chen, Y. Cui, R. A. Vilá, D. T. Boyle, Y. Cui, *Science* **2024**, *386*, 322.
[37] C. Cockreham, J. Rosener, S. A. Hawks, E. Glascoe, *ACS Omega* **2025**, *10*, 10294.
[38] M. Ghasemifard, S. M. Hosseini, G. H. Khorrami, *Ceram. Int.* **2009**, *35*, 2899.
[39] C. Qiu, B. Wang, N. Zhang, S. Zhang, J. Liu, D. Walker, Y. Wang, H. Tian, T. R. Shrout, Z. Xu, L.-Q. Chen, F. Li, *Nature* **2020**, *577*, 350.
[40] F. Lin, Z. Li, B. Sun, W. Peng, Z. Cao, K. Gao, Y. Cui, K. Zhu, Q. Lu, J. Li, Y. Lyu, F. Ren, *Mater. Today Adv.* **2024**, *22*, 100506.
[41] L. Chen, *J. Am. Ceram. Soc.* **2008**, *91*, 1835.
[42] V. V. Shvartsman, D. A. Kiselev, A. V. Solnyshkin, D. C. Lupascu, M. V. Silibin, *Sci. Rep.* **2018**, *8*, 378.
[43] Q. Chen, Y. Shen, S. Zhang, Q. M. Zhang, *Annu. Rev. Mater. Res.* **2015**, *45*, 433.
[44] T. Yamada, T. Ueda, T. Kitayama, *J. Appl. Phys.* **1982**, *53*, 4328.
[45] J. Tang, J. Liu, H. Huang, *J. Electron. Mater.* **2019**, *48*, 4033.
[46] G. Zhang, P. Zhao, X. Zhang, K. Han, T. Zhao, Y. Zhang, C. K. Jeong, S. Jiang, S. Zhang, Q. Wang, *Energy Environ. Sci.* **2018**, *11*, 2046.
[47] X. Du, Z. Zhou, Z. Zhang, L. Yao, Q. Zhang, H. Yang, *J. Adv. Ceram.* **2022**, *11*, 331.
[48] A. Sasmal, A. Patra, P. Maiti, S. Sen, A. Arockiarajan, *ACS Appl. Electron. Mater.* **2025**, *7*, 4540.
[49] P. Li, W. Jiang, R. Lu, D. Yuan, J. Shan, J. Xiao, *Constr. Build. Mater.* **2022**, *323*, 126621.
[50] X. Zhang, W. Xia, J. Liu, M. Zhao, M. Li, J. Xing, *J. Electron. Mater.* **2022**, *51*, 5528.
[51] J. Lee, S. Lim, *J. Ind. Eng. Chem.* **2018**, *67*, 478.
[52] F.-A. He, K. Lin, D.-L. Shi, H.-J. Wu, H.-K. Huang, J.-J. Chen, F. Chen, K.-H. Lam, *Compos. Sci. Technol.* **2016**, *137*, 138.
[53] S. Zhang, W. Tong, J. Wang, W. Wang, Z. Wang, Y. Zhang, *J. Appl. Polym. Sci.* **2020**, *137*, 48412.
[54] L. Yang, Q. Zhao, Y. Hou, L. Hong, H. Ji, L. Xu, K. Zhu, M. Shen, H. Huang, H. He, J. Qiu, *Compos. Sci. Technol.* **2019**, *174*, 33.
[55] Y. J. Choi, M.-J. Yoo, H.-W. Kang, H.-G. Lee, S. H. Han, S. Nahm, *J. Electroceram.* **2013**, *30*, 30.
[56] C. Liu, H. Xu, B. Huo, J. Wang, Z. Wang, X. Chen, F. Meng, C. Sun, Y. Wang, *J. Water Process Eng.* **2023**, *55*, 104181.
[57] G. Tian, W. Deng, T. Yang, J. Zhang, T. Xu, D. Xiong, B. Lan, S. Wang, Y. Sun, Y. Ao, L. Huang, Y. Liu, X. Li, L. Jin, W. Yang, *Adv. Mater.* **2024**, *36*, 2313612.
[58] Y. Zi, L. Lin, J. Wang, S. Wang, J. Chen, X. Fan, P. Yang, F. Yi, Z. L. Wang, *Adv. Mater.* **2015**, *27*, 2340.
[59] S.-H. Jo, S.-G. Lee, S.-H. Lee, *Mater. Res. Bull.* **2012**, *47*, 409.
[60] B. Sharma, A. Sharma, R. Gupta, A. Chowdhuri, M. Verma, M. Tomar, *Ceram. Int.* **2024**, *50*, 46982.
[61] M. Olszowy, C. Pawlaczyk, E. Markiewicz, J. Kułek, *Phys. Status Solidi A* **2005**, *202*, 1848.
[62] R. I. Mahdi, W. H. Abd Majid, *RSC Adv.* **2016**, *6*, 81296.
[63] Y. Wang, H. Ye, P. Wang, Z. Wu, Q. Guan, C. Zhang, H. Li, S. Chen, J. Luo, *Adv. Mater.* **2024**, *36*, 2409245.
[64] B. Zhang, C. Guo, X. Cao, X. Yuan, X. Li, H. Huang, S. Dong, Z. L. Wang, K. Ren, *Nano Energy* **2022**, *104*, 107897.
[65] H. Tang, X. Niu, P.-F. Zhao, X.-G. Tang, X.-D. Jian, X.-Y. Chen, X.-C. Peng, Z.-P. Yang, S.-G. Lu, *J. Mater. Chem. C* **2022**, *10*, 1302.
[66] A. K. Batra, M. D. Aggarwal, M. E. Edwards, A. Bhalla, *Ferroelectrics* **2008**, *366*, 84.
[67] S. Li, Y. Wang, Z. Liu, B. Chen, M. Liu, X. He, S. Yang, *Sci. Adv.* **2025**, *11*, adt6136.
[68] L. Wu, Z. Jin, Y. Liu, H. Ning, X. Liu, N. H. Alamusi, *Nanotechnol. Rev.* **2022**, *11*, 1386.
[69] N. Khakpash, H. Khassaf, G. A. Rossetti, S. P. Alpay, *Appl. Phys. Lett.* **2015**, *106*, 082905.
[70] A. K. Tagantsev, *Ferroelectrics* **2008**, *375*, 19.
[71] S. Y. Hu, L. Q. Chen, *Acta Mater.* **2001**, *49*, 1879.